nature materials

LETTERS

PUBLISHED ONLINE: 1 JUNE 2015 | DOI: 10.1038/NMAT4320

Three-dimensional imaging of dislocation propagation during crystal growth and dissolution

Jesse N. Clark[1*†‡], Johannes Ihli[2‡], Anna S. Schenk[2], Yi-Yeoun Kim[2], Alexander N. Kulak[2], James M. Campbell[3], Gareth Nisbet[4], Fiona C. Meldrum[2*] and Ian K. Robinson[1,5]

Atomic-level defects such as dislocations play key roles in determining the macroscopic properties of crystalline materials[1,2]. Their effects range from increased chemical reactivity[3,4] to enhanced mechanical properties[5,6]. Dislocations have been widely studied using traditional techniques such as X-ray diffraction and optical imaging. Recent advances have enabled atomic force microscopy to study single dislocations[7] in two dimensions, while transmission electron microscopy (TEM) can now visualize strain fields in three dimensions with near-atomic resolution[8–10]. However, these techniques cannot offer three-dimensional imaging of the formation or movement of dislocations during dynamic processes. Here, we describe how Bragg coherent diffraction imaging (BCDI; refs 11,12) can be used to visualize in three dimensions, the entire network of dislocations present within an individual calcite crystal during repeated growth and dissolution cycles. These investigations demonstrate the potential of BCDI for studying the mechanisms underlying the response of crystalline materials to external stimuli.

Crystal growth and dissolution processes have been studied for over a century[13], owing to their significance to fields such as geology, corrosion, catalysis and the synthesis of nanostructures, a desire to understand the link between microscopic and macroscopic processes, and to our innate fascination with such structures. These investigations confirmed that dissolution and growth proceed by analogous mechanisms[14] and also identified that crystallographic defects, and in particular screw dislocations, are of fundamental importance to crystal growth and dissolution processes[15]. This can be attributed to the fact that screw dislocations cause deformation (and therefore strain) of the adjacent crystal lattice, which in turn alters the activation barrier for growth and dissolution in the vicinity of the dislocation[16]. A full picture of crystal growth and dissolution mechanisms can therefore be obtained only by studying the relationship between the evolution of the network of dislocations within a crystal and its morphology during these processes.

In this article, we demonstrate how BCDI (refs 17,18) can be used to study the role of dislocations in dictating the mechanism of growth and dissolution of calcite crystals. Calcite was selected for study as it is one of the most-studied inorganic crystals, and the crystals readily grow to a few micrometres in size, with well-defined morphologies. BCDI is an imaging technique that uses coherent X-rays to image the density (and morphology) of a crystal and, importantly, the strain within it[11,12]. Illumination of a crystal that is smaller than the coherence volume of the beam generates a coherent X-ray diffraction (CXD) pattern due to scattering from all parts of the crystal. An image of the crystal morphology can then be generated from the CXD pattern, where the phase of the scattered wave is reconstructed using iterative phase retrieval algorithms[11,12,17–19]. The reconstructed density is complex valued, with the amplitude containing information about the electron density, $\rho(\mathbf{r})$. Phase shifts in the reconstructed complex density arise from strain (internal deformation) in the crystal lattice. The phase is proportional to the vector displacement field, $\mathbf{u}(\mathbf{r})$ of the atoms from the ideal lattice points and the scattering vector $\mathbf{Q}$ via $\phi(\mathbf{r}) = \mathbf{Q} \cdot \mathbf{u}(\mathbf{r})$ (see Supplementary Information). For a single Bragg peak, a single projection of $\mathbf{u}$ is obtained and components of $\mathbf{u}$ perpendicular to $\mathbf{Q}$ will not be observed. It is this sensitivity to deformations that makes BCDI ideal for studying defects within crystals.

Calcite crystals were precipitated by placing 100 µl droplets of a solution containing $CaCl_2$, urea and urease on hydroxyl-terminated, self-assembled monolayers (SAMs) supported on thin gold films (see Methods). $CaCO_3$ precipitation then occurred on enzymatic hydrolysis of the urea to ammonium and carbonate[20]. This method was selected as it generated a high density of {104} oriented calcite rhombohedra with average diameters of ≈1.25 µm (ref. 21). BCDI experiments were carried out at beamline I16 at the Diamond Light Source. Individual calcite crystals below 2 µm in size were illuminated with monochromatic, 8 keV X-rays, and diffraction was recorded at the {104} Bragg peak (see Methods). Three-dimensional (3D) diffraction data sets (Supplementary Fig. 1) were obtained by rocking an isolated calcite crystal through its Bragg peak, and the same crystal was monitored while undergoing cycles of growth and dissolution. Dissolution was achieved by depositing dilute acetic acid solution on the crystal, whereas growth was achieved by adding a drop of calcium bicarbonate solution (see Methods). Alignment of the crystal was maintained throughout, as the X-rays were nominally unfocussed and defined by slits with a square opening of 200 µm placed 0.3 m before the sample. This large beam size relative to crystal size also ensured that the sample was coherently illuminated[22].

Figure 1 shows 3D images of the crystals as iso-surface renderings of the reconstructed amplitudes (electron density, see Supplementary Information; Fig. 1a–d) and phase (projected lattice displacement; Fig. 1e–h) of the initial crystal (Fig. 1a,e, stage i), after growth (Fig. 1b,f, stage ii) and after two consecutive dissolution steps (Fig. 1c,g, stage iii, and d,h, stage iv). The initial crystal (Fig. 1a)

[1]London Centre for Nanotechnology, University College London, London WC1E 6BT, UK. [2]School of Chemistry, University of Leeds, Leeds LS2 9JT, UK. [3]School of Physics and Astronomy, University of Leeds, Leeds LS2 9JT, UK. [4]Diamond Light Source, Harwell Science and Innovation Campus, Didcot, Oxon OX11 0DE, UK. [5]Research Complex at Harwell, Didcot, Oxfordshire OX11 0DE, UK. †Present addresses: Stanford PULSE Institute, SLAC National Accelerator Laboratory, 2575 Sand Hill Road, Menlo Park, California 94025, USA; Center for Free-Electron Laser Science (CFEL), Deutsches Elektronensynchrotron (DESY), Notkestrasse 85, 22607 Hamburg, Germany. ‡These authors contributed equally to this work.
*e-mail: jesclark@stanford.edu; F.Meldrum@leeds.ac.uk

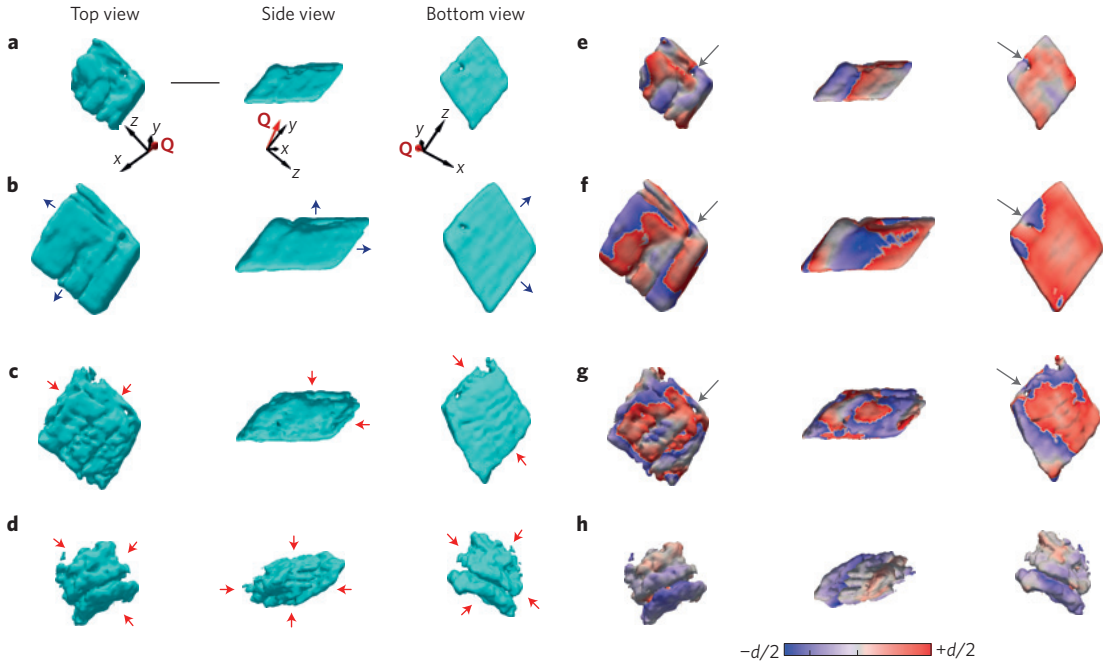

Figure 1 | Growth and dissolution of calcite observed by BCDI. a–h, Iso-surface rendering of the electron density (reconstructed amplitude) (**a**–**d**) and projected displacement (phase) (**e**–**h**) from initially deposited calcite crystal (**a**,**e**, stage i), after secondary growth (**b**,**f**, stage ii), and after consecutive dissolution steps (**c**,**g**, stage iii, and **d**,**h**, stage iv). The scale bar is 1 μm. Three different viewing angles of the crystal are shown—top down, side and bottom up. The substrate would be on the bottom of the crystal shown in the side view. Perspectives highlight the shape transition that occurs during growth (**a**,**b** and **e**,**f**) and dissolution (**b**–**d** and **f**–**h**). Prominent surface advance (growth, blue arrows) and retreat (dissolution, red arrows) directions are shown. The grey arrow points towards the primary dislocation continuously identifiable during crystal growth and dissolution (**a**–**c** and **e**–**g**). The beam direction is along the *z* axis, with the *y* axis vertical. The scattering vector (**Q**) is shown in red.

is the expected rhombohedron, which is consistent with scanning electron micrographs (Supplementary Fig. 3). Growth of this crystal (Fig. 1b,c) leads to an increase in size and a smoothing of the faces exposed to the bulk solution, whereas the face in contact with the SAM remains unchanged. Interestingly, two of the faces directed into the solution (indicated with blue arrows) grow more rapidly than the other three. This is immediately indicative of a non-uniform distribution of defects, as all faces of an entirely perfect rhombohedron would be expected to grow at the same rate. Images of the corresponding projected displacements are shown in Fig. 1e–h, where this is mapped onto an iso-surface with red and blue representing lattice contraction or expansion respectively by half a lattice spacing. Comparison of the projected displacements before (Fig. 1e) and after (Fig. 1f) crystal growth shows that these do not grow significantly with the crystal but remain maximal at the edges. This is indicative of the presence of active growth fronts[23].

The dissolution steps (Fig. 1b,c and c,d) show that the crystal faces retreat along all directions, but is more pronounced at certain sites (indicated by red arrows). Initial signs of changes in the crystal shape and the onset of etch-pit formation are visible after the first stage of dissolution (Fig. 1c), leading to an increase in the specific surface area and roughness of the crystal. The etch pits are also associated with higher levels of deformation/strain (Fig. 1g). That relatively little change occurs in the crystal face adjacent to the substrate is consistent with the intimate contact of the SAM with this nucleation face. The second dissolution step (Fig. 1c,d) results in a significant change in the crystal morphology, and the production of a porous isometric form[24] that is quite distinct from the original shape, and which can be attributed to the removal of defect outcrops at the crystal surface and the coinciding etch pits formed[25,26]. Looking at the lattice deformation, it is evident that strain present at the crystal surface reduces with the increased dissolution. This indicates that the least stable (more strained) regions dissolve first, leaving behind a more stable core (Supplementary Movies 1–4).

The projected displacement images also reveal a further feature, which is indicated by the grey arrows in Fig. 1e–g, and is present throughout the growth and dissolution of the crystal. This region possesses both a hollow core and a spiral phase, where this combination of features is characteristic of dislocations and agrees with 2D images of dislocations obtained with TEM (ref. 8) and Bragg ptychography[27]. A number of these dislocations are highlighted in Fig. 2. Dislocations are characterized by a Burgers vector that measures the topological shift of the crystal along the dislocation line, where this is usually a lattice vector of the crystal[28]. Whenever there is a component of the Burgers vector parallel to the dislocation line, it has a screw dislocation character causing the lattice to spiral around the dislocation; in this way crystal growth (and dissolution) can be facilitated. Confirmation that this feature indeed corresponds to a screw dislocation was obtained by recording the polar angle dependence of the displacement associated with the core (indicated by the circles in Fig. 2) over the growth/ dissolution cycle of the crystal (Fig. 3a). Although calcite is elastically anisotropic, an approximately linear relationship was observed and is consistent with what is predicted by linear elasticity theory[28] (see Supplementary Information). To further confirm the nature of the identified dislocation, a comparison is provided between a simulated screw dislocation and simulated screw after BCDI processing. The model screw dislocation used in the simulation is shown at atomic resolution in Fig. 4a, with the resulting displacement of atoms from their ideal lattice positions given in Fig. 4c. The BCDI experiment simulated screw dislocation is shown in Fig. 4b,d (see Supplementary Information). Figure 4e,f provide a comparison of BCDI-reconstructed displacement and simulated displacement, viewed along the dislocation line, and clearly show that the low-density core and spiral displacement are well-preserved after BCDI processing.

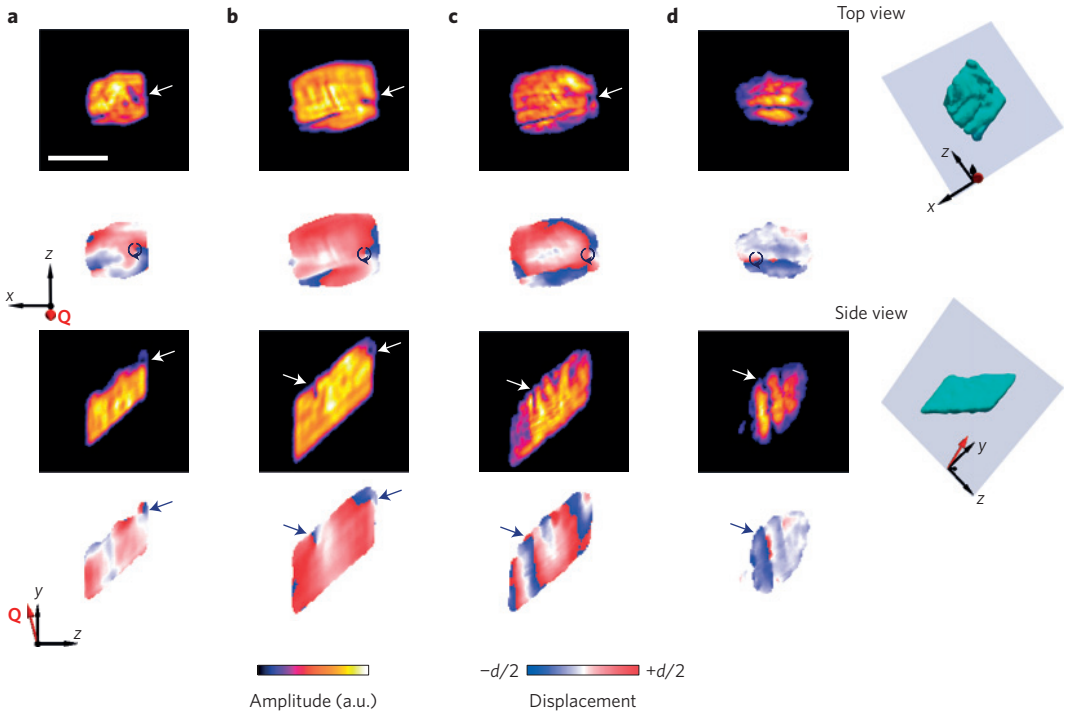

Figure 2 | Slices showing the electron density and projected displacement during growth and dissolution. a–d, Crystal in the initial state (**a**), and after growth (**b**) and repetitive dissolution steps (**c**,**d**) for two viewing directions (top view) and (side view). The amplitude is shown in the top rows (black background) with the dislocations highlighted by white arrows featuring a low-amplitude core. The phase presented in the bottom rows also shows selected dislocations highlighted by the dark blue arrows. Particularly evident is the spiral phase (displacement) that is characteristic of a screw dislocation. The iso-surface to the right shows the location of the cut planes. The scale bar is 1 μm.

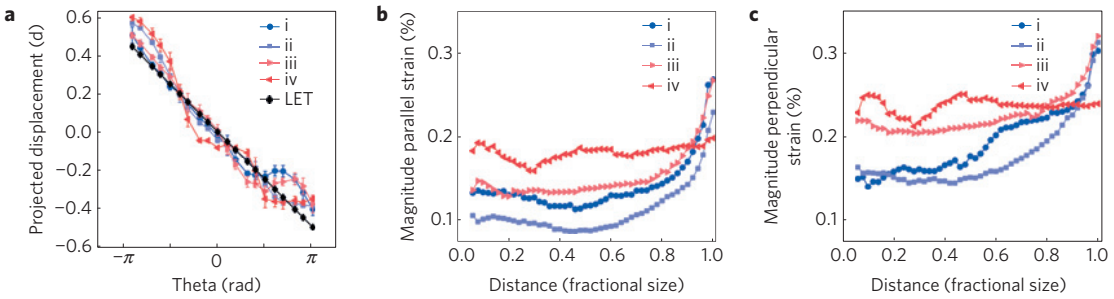

Figure 3 | Displacement and strain magnitude line plots. a, Recovered projected displacement measured at development stages (i–iv) as a function of theta for the dark blue circles with arrows from Fig. 2a. This is compared to the displacement expected by linear elasticity theory (LET). The error bars represent the standard deviation ($\pm\sigma$) of the displacement over adjacent layers spanning a region of 200 nm along **Q**. **b**,**c**, The magnitude of the strain component parallel (**b**) and perpendicular (**c**) to the scattering vector over the growth/dissolution cycle (i–iv) plotted as a function of fractional crystal size (centre of the crystal 0 to crystal surfaces 1). These graphs highlight the diminishing relevance of surface effects with growth (ii) of the crystal, and its increasing relevance with dissolution (iii and iv). The strain is calculated as the magnitude of the gradient of the displacement and averaged over successively larger shells.

Further examination of regions that showed a spiral deformation and low-amplitude core enabled many more dislocations to be identified within the imaged crystal (see Supplementary Information). These have been rendered and are shown in Fig. 5 and Supplementary Movies 5–8. In many cases the exact type of dislocation cannot be identified from a single Bragg reflection, as edge, screw and mixed dislocations will all possess qualitatively similar deformation fields. The initial crystal (Fig. 5a) possesses several dislocations which are located relatively close to the crystal surface (down to 200 nm) and are found predominantly parallel to {104} planes. These dislocations are mainly associated with the faces exposed to the bulk solution, and are visible throughout a single crystal growth and dissolution cycle (Fig. 5a–c), during which they increase (Fig. 5b) and decrease (Fig. 5c) in length. The reproducibility of locating the same dislocation across independently reconstructed data sets provides further credence to the recovered images.

Dislocations are often found to occur in loops or pairs with opposite Burgers vector, as this reduces the lattice potential energy and resulting long-range strain associated with these features. They also are stabilized near crystal surfaces, as found in this work, such that dislocation motion can transport material into and out of crystals from the growth solution[29]. As intuitively expected, the most rapidly growing crystal faces were observed to have the highest number of surface dislocations. The distribution of these defects within the crystal therefore plays a part in determining the morphology of the product crystal. Considering the dissolution

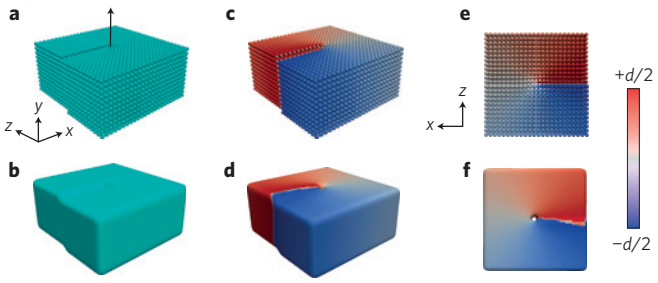

Figure 4 | Simulation of a screw dislocation. **a**, Iso-surface rendering of a screw dislocation with atomic resolution. **b**, Iso-surface rendering by filtering the Fourier transform of **a** with a Gaussian centred on the (0,1,0) Bragg peak, replicating the BCDI experiment. **c**,**d**, The displacement is rendered onto the iso-surface for the atomic resolution (**c**) and the phase is rendered onto the surface for the BCDI simulation (**d**) showing the spiral phase centred around the dislocation core. **e**,**f**, Another view of the dislocation for the atomic resolution (**e**) and BCDI experiment (**f**), revealing the low-density region at the core in the BCDI experiment simulation. It should be noted that for the atomic resolution the displacement is mapped onto the iso-surface, whereas for the BCDI example the resultant phase is mapped onto the iso-surface.

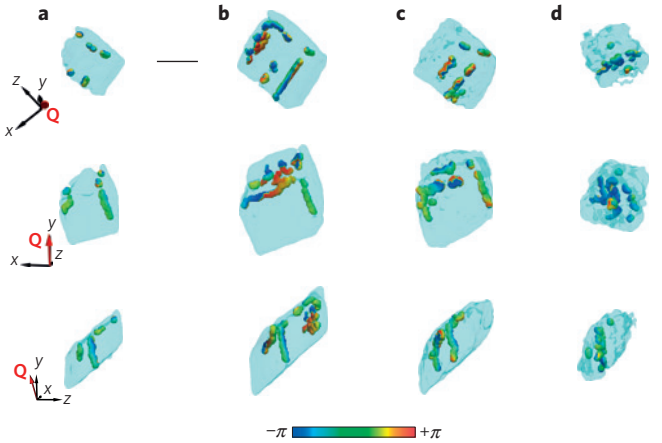

Figure 5 | Iso-surface rendering of defect network within a calcite crystal. **a**–**d**, Iso-surface renderings of dislocations present within the crystal imaged before (**a**) and after (**b**) growth, and after dissolution (**c**,**d**). The scale bar is 1 μm. The evolution of the dislocations is evident through crystal growth (**a**,**b**) and dissolution (**b**,**c** and **c**,**d**), where these are shown from left to right. Three different viewing angles of the crystals are provided (vertically, top to bottom)—from the base, above and the side. Dislocations are predominantly located near the surface and on the faces that grow most rapidly. The phase has been mapped to the iso-surfaces of present dislocations, showing the characteristic spiral.

process, the locations of the dislocations coincide with the position of the etch pits that appear at the crystal surface during dissolution. This suggests that the developing pits follow the cores of the dislocations, where this effect can be attributed to a reduced activation barrier to dissolution due to stored strain energy in the defects[14]. New dislocations could be identified during the dissolution (Fig. 5c,d), and by the final stage (Fig. 5d) many of the original dislocations had been annihilated. The loss of faceting and dislocations near the surface support the hypothesis that the least stable regions dissolve first, leaving behind a more stable core.

To determine the overall effect that the growth/dissolution had on the strain and deformation of the crystal, the gradient of the displacement was calculated and its magnitude was plotted as a function of fractional size (Fig. 3b,c). The magnitude of the gradient was calculated over successively larger shells, averaged over all directions, and is plotted as a percentage of deformation (strain) relative to the lattice constant for the {104} reflection (see Supplementary Information) for the directions parallel and perpendicular to the scattering vector. What is evident (Fig. 3b,c) is that the initial crystallite experiences an increasing strain from the centre, outwards. This can be compared to a crystal formed after the first growth stage (Fig. 1f), which shows an overall flatter initial strain, and then increases more rapidly above a fractional size ≈0.6. The smoother transition and lower strain for the direction parallel suggest some relaxation of the crystal after the initial growth and can also be seen in the slices in Fig. 2. The non-zero strain perpendicular to the scattering vector is indicative of a shear strain, although we have only a single Bragg peak so the full strain tensor cannot be obtained and the exact nature of this cannot be determined. These data are consistent with the assertion that the effect of the surface penetrates only to a finite distance into a crystal. With the increased roughness and etch-pit formation that occurs in the first dissolution step (Fig. 1g), the overall strain is higher, demonstrating that these surface features affect the entire crystal, leading to an increase in overall deformation. After the final dissolution (Fig. 1h), when the majority of surface dislocations have been removed, the strain becomes almost flat. This indicates that surface effects are less pronounced, despite the increased relative surface area.

With its ability to simultaneously generate 3D images of the strain within a crystal and the gross crystal morphology, BCDI provides an extremely powerful way of visualizing the network of dislocations present within an individual crystal. Importantly, BCDI can be performed in the absence of any sample preparation, which means that it can be used to elucidate the effects of dislocation networks on dynamic crystal behaviour. Using the example of crystal growth and dissolution, we have located dislocations within calcite single crystals, and then demonstrated that their distribution within the crystal dictates rapidly growing directions. Conversely, preferential dissolution and etch-pit formation was also observed within the vicinity of the dislocations, which provides evidence that the stored energy within the dislocations affects the crystal response. The ability to view these fundamental processes using BCDI represents an important step forward in elucidating the nanoscale mechanisms underlying crystallization processes. Importantly, BCDI also opens the door to 3D visualization of the role of dislocations in the response of a crystal to a huge range of experimental conditions, such as temperature changes or mechanical force.

Methods

Methods and any associated references are available in the online version of the paper.

Received 12 January 2015; accepted 4 May 2015; published online 1 June 2015

References

1. Stoneham, A. *Theory of Defects in Solids* (Clarendon, 1985).
2. Burton, C. A theory concerning the constitution of mater. *Phil. Mag.* **33,** 191–203 (1892).
3. Lasaga, A. C. & Luttge, A. Variation of crystal dissolution rate based on a dissolution stepwave model. *Science* **291,** 2400–2404 (2001).
4. De Yoreo, J. J. & Vekilov, P. G. Principles of crystal nucleation and growth. *Rev. Mineral. Geochem.* **54,** 57–93 (2003).
5. Ma, E., Shen, T. D. & Wu, X. L. Nanostructured metals: Less is more. *Nature Mater.* **5,** 515–516 (2006).
6. Kunitake, M. E., Mangano, L. M., Peloquin, J. M., Baker, S. P. & Estroff, L. A. Evaluation of strengthening mechanisms in calcite single crystals from mollusk shells. *Acta Biomater.* **9,** 5353–5359 (2013).
7. Davis, K. J., Dove, P. M. & De Yoreo, J. J. The role of Mg^{2+} as an impurity in calcite growth. *Science* **290,** 1134–1137 (2000).
8. Hÿtch, M. J., Putaux, J-L. & Penisson, J-M. Measurement of the displacement field of dislocations to 0.03 Å by electron microscopy. *Nature* **423,** 270–273 (2003).

9. Barnard, J. S., Sharp, J., Tong, J. R. & Midgley, P. A. High-resolution three-dimensional imaging of dislocations. *Science* **313,** 319 (2006).
10. Chen, C-C. *et al.* Three-dimensional imaging of dislocations in a nanoparticle at atomic resolution. *Nature* **496,** 74–77 (2013).
11. Pfeifer, M. A., Williams, G. J., Vartanyants, I. A., Harder, R. & Robinson, I. K. Three-dimensional mapping of a deformation field inside a nanocrystal. *Nature* **442,** 63–66 (2006).
12. Robinson, I. & Harder, R. Coherent X-ray diffraction imaging of strain at the nanoscale. *Nature Mater.* **8,** 291–298 (2009).
13. Weeks, J. D. & Gilmer, G. H. *Advances in Chemical Physics* 157–228 (John Wiley, 2007).
14. Dove, P. M. & Han, N. Kinetics of mineral dissolution and growth as reciprocal microscopic surface processes across chemical driving force. *AIP Conf. Proc.* **916,** 215–234 (2007).
15. Frank, F. C. The influence of dislocations on crystal growth. *Discuss. Faraday Soc.* **5,** 48–54 (1949).
16. Brantley, S. L. in *Kinetics of Water-Rock Interaction* (eds Brantley, S. L., Kubicki, J. D. & White, A. F.) 151–210 (Springer, 2008).
17. Clark, J. N. *et al.* Ultrafast three-dimensional imaging of lattice dynamics in individual gold nanocrystals. *Science* **341,** 56–59 (2013).
18. Cha, W. *et al.* Core–shell strain structure of zeolite microcrystals. *Nature Mater.* **12,** 729–734 (2013).
19. Fienup, J. R. Phase retrieval algorithms: A comparison. *Appl. Opt.* **21,** 2758–2769 (1982).
20. Antipov, A. *et al.* Urease-catalysed carbonate precipitation inside the restricted volume of polyelectrolyte capsules. *Macromol. Rapid Commun.* **24,** 274–277 (2003).
21. Lee, J. R. I. *et al.* Structural development of mercaptophenol self-assembled monolayers and the overlying mineral phase during templated $CaCo_3$ crystallization from a transient amorphous film. *J. Am. Chem. Soc.* **129,** 10370–10381 (2007).
22. Clark, J. N., Huang, X., Harder, R. & Robinson, I. K. High-resolution three-dimensional partially coherent diffraction imaging. *Nature Commun.* **3,** 993 (2012).
23. Paquette, J. & Reeder, R. J. Relationship between surface structure, growth mechanism, and trace element incorporation in calcite. *Geochim. Cosmochim. Acta* **59,** 735–749 (1995).
24. Snyder, R. C. & Doherty, M. F. Faceted crystal shape evolution during dissolution or growth. *AIChE J.* **53,** 1337–1348 (2007).
25. MacInnis, I. N. & Brantley, S. L. The role of dislocations and surface morphology in calcite dissolution. *Geochim. Cosmochim. Acta* **56,** 1113–1126 (1992).
26. MacInnis, I. N. & Brantley, S. L. Development of etch pit size distributions on dissolving minerals. *Chem. Geol.* **105,** 31–49 (1993).
27. Takahashi, Y. *et al.* Bragg X-ray ptychography of a silicon crystal: Visualization of the dislocation strain field and the production of a vortex beam. *Phys. Rev. B* **87,** 121201 (2013).
28. Hirth, J. P. & Lothe, J. *Theory of Dislocations* (McGraw-Hill, 1968).
29. Pun, G. P. & Mishin, Y. A molecular dynamics study of self-diffusion in the cores of screw and edge dislocations in aluminum. *Acta Mater.* **57,** 5531–5542 (2009).

Acknowledgements

This work was supported by FP7 advanced grant from the European Research Council (J.N.C. and I.K.R.) and an Engineering and Physical Sciences Research Council Leadership Fellowship (F.C.M. and J.I.). It was also funded through an EPSRC Programme Grant (A.S.S. and F.C.M., EP/I001514/1) which funds the Materials in Biology (MIB) consortium, and EPSRC grants EP/J018589/1 (Y-Y.K.) and EP/K006304/1 (A.N.K.). We thank Diamond Light Source for access to Beamline I-16 (MT 8187, MT 7654 and MT 7277) that contributed to the results presented here.

Author contributions

J.N.C. and J.I. designed the project; J.I. prepared samples; J.N.C., J.I., J.M.C., A.S.S., Y-Y.K., J.M.C., G.N. and I.K.R. performed the experiments; J.N.C. performed image reconstructions; J.N.C. and I.K.R. analysed the data, J.N.C., J.I., F.C.M. and I.K.R. wrote the paper. All the authors read and commented on the manuscript.

Additional information

Supplementary information is available in the online version of the paper. Reprints and permissions information is available online at www.nature.com/reprints. Correspondence and requests for materials should be addressed to J.N.C. or F.C.M.

Competing financial interests

The authors declare no competing financial interests.

Methods

Materials and general preparative methods. Analytical grade, $CaCl_2 \cdot 2H_2O$, acetic acid, urea and urease (*Canavalia ensiformis*, subunit molecular weight: ~90.770 kDa) were purchased from Sigma-Aldrich and were used as received. Aqueous solutions were prepared using Milli-Q Standard 18.2 MΩ cm. Solutions of 11-mercapto-1-undecanol (Sigma-Aldrich) were freshly prepared in laboratory grade ethanol, and experiments were performed at a constant temperature of 21 °C. Reagent-containing glassware was soaked overnight in 10% w/v NaOH, followed by rinsing with dilute HCl and washing with Milli-Q water.

Substrate preparation. Glass slides and crystallizing dishes were placed overnight in piranha solution (70:30 wt%. sulphuric acid: hydrogen peroxide) and were then washed copiously with Milli-Q water before being exposed to the crystallization solution. Functionalized self-assembled monolayers (SAMs) were prepared on freshly deposited noble metal films. Thin films were deposited either on silicon wafers using a Mantis Qprep 250 deposition system or a Cressington 308R coating system at a base pressure below 10^{-6} mbar. 2 nm of Cr were initially deposited to promote substrate adhesion, followed by the evaporation of 50 nm of Au (Goodfellow, 99.99%) at $\leq$0.1 nm s^{-1}. SAMs were then prepared by immersing a prepared metal substrate in 1 mM thiol solution in ethanol, at room temperature for 24 h in the dark. The SAMS were then thoroughly rinsed with ethanol and Milli-Q water and were dried under nitrogen before usage.

Mineral deposition. Preferentially oriented calcite was obtained by adding 350 µl urease (1 mg ml^{-1}) to 1 ml of 5 mM $CaCl_2$/20 mM urea. Separate droplets (100 µl) of the resulting aqueous solution were subsequently placed on the prepared SAM, and stored at 100% r.h. Hydroxyl-terminated SAMs were used as the crystallization substrate to obtain calcite rhombohedra that were principally {104} oriented. Enzymatic hydrolysis of urea to ammonium and carbonate creates the required supersaturation profile, where the gradual increase in supersaturation ensures that a sufficient density of single-crystal particles of $CaCO_3$ is obtained.

Overgrowth of initial deposits. Observations of crystal growth were carried out on samples which had previously been centred into the Bragg condition. A 50 µl volume of approximately 1 mM calcium bicarbonate solution was pipetted onto the sample, where evaporation and CO_2 out-gassing results in a supersaturation increase which causes crystal growth. After evaporation of the droplet, the selected crystals were then reanalysed. Calcium bicarbonate solutions were prepared according to the method of Kitano[30]. 100 mg of $CaCO_3$ were added to one litre of Milli-Q water. $CO_{2(g)}$ was then bubbled through this solution for three hours followed by filtering through a 200 nm Isopore GTTP membrane filter (Millipore), resulting in an initial pH of 6.4.

Partial dissolution. Dissolution of BCDI-imaged calcite crystals was achieved by depositing 50 µl of 0.1 wt% acetic acid solution onto a 0.4 cm^2 substrate with an estimated number density of 0.1 crystals μm^{-2} with an average size of 1 µm. The solution was then removed after 60 s. This was followed by addition and removal of a drop of ethanol to wash the sample, and a further diffraction pattern was collected (see Supplementary Fig. 4). The process was then repeated either two and three times to obtain diffraction data for successive dissolution stages of the initially imaged single crystal.

Enzymatic hydrolysis (urea–urease) catalysed precipitation. Calcium carbonate deposition using the enzymatic hydrolysis of urea by urease, and droplets placed on the substrate, allows controlled precipitation of crystals independent of droplet wetting behaviour and gas–liquid interface area[31]. By variation of the urea and urease concentrations, which determine the rate of production of carbonate and ammonium, the rate of production of $CaCO_3$ can be controlled. A slow increase in supersaturation was required to give crystals that were principally unstrained and which were present in a high enough number density to enable crystals to be easily located on the substrate during BCDI imaging. The key underlying reactions are presented below.

$$((NH_2)_2CO) + 2H_2O \xrightarrow{\text{Urease}} 2(NH_4^+) + (CO_3^{2-})$$

$$((NH_2)_2CO) + H_2O \xrightarrow{\text{or}} 2(NH_3) + (CO_2)$$

$$(NH_3) + H_2O \leftrightarrow (NH_4^+) + OH^-$$

$$(CO_2^-) + H_2O \leftrightarrow (H_2CO_3)$$

$$(H_2CO_3) \leftrightarrow (HCO_3^-) + (H^+)$$

$$(HCO_3^-) \leftrightarrow (CO_3^{2-}) + (H^+)$$

$$(CO_3^{2-}) + (Ca^{2+}) \leftrightarrow CaCO_3$$

External characterization. $CaCO_3$ precipitates at different growth and dissolution stages were characterized by scanning electron microscopy (SEM). Electron micrographs of uncoated specimen were obtained using a FEI Nova NanoSEM 650. Crystal growth and dissolution rates of outgrown individual calcite crystal were obtained using an inverted Olympus IX-70 confocal microscope.

Experimental set-up. BCDI experiments were performed at Beamline I-16 at the Diamond Light Source (DLS) UK. An undulator produced X-rays which were monochromatized to an energy of 8 keV using a channel-cut Si(111) monochromator. Calcite crystals supported on substrates were placed on a diffractometer which had its rotation centre aligned with the X-ray beam. Slits were used to reduce the area illuminated by the X-rays. An X-ray-sensitive, CMOS pixel detector (Medipix3) with 256 × 256 square pixels of side length 55 µm was positioned at the desired diffraction angle for an off-specular {104} reflection at a distance of 2.7 m from the sample. An evacuated flight tube was placed between the detector and sample to reduce air absorption and scatter. To measure its full 3D diffraction pattern, the crystal was rotated by 0.3° with a 0.003° step size. A two-dimensional slice of the 3D far-field diffraction pattern was recorded at each angle of rotation using an exposure time of 1 s. By stacking all of these 2D diffraction frames together, a complete 3D diffraction pattern was obtained, from which real-space images can be reconstructed (see Supplementary Information). Owing to the small size of the crystals (~1–2 µm) the illumination can be considered to be almost completely coherent. To ensure that the same crystal could be analysed over a growth/dissolution cycle, a local search in reciprocal space was performed to pick an isolated single crystal. This ensured that there was little chance of a signal originating from another crystal overlapping the original crystal diffraction.

References

30. Kitano, Y., Park, K. & Hood, D. W. Pure aragonite synthesis. *J. Geophys. Res.* **67,** 4873–4874 (1962).
31. Ihli, J., Bots, P., Kulak, A., Benning, L. G. & Meldrum, F. C. Elucidating mechanisms of diffusion-based calcium carbonate synthesis leads to controlled mesocrystal formation. *Adv. Funct. Mater.* **23,** 1965–1973 (2013).